

Supplement of Atmos. Chem. Phys., 19, 1623–1647, 2019
<https://doi.org/10.5194/acp-19-1623-2019-supplement>
© Author(s) 2019. This work is distributed under
the Creative Commons Attribution 4.0 License.



Supplement of

The role of low-level clouds in the West African monsoon system

Anke Kniffka et al.

Correspondence to: Anke Kniffka (anke.kniffka@kit.edu)

The copyright of individual parts of the supplement might differ from the CC BY 4.0 License.

S1 Supplementary Material

S1.1 Climatology and model evaluation

In addition to the general characterization of the meteorological conditions in southern West Africa for the variables precipitation and radiation, a brief discussion about the diurnal cycle of the vertical atmospheric structure is given for the wet monsoon season July, August and September 2006. Comparison of ICON CLIM with ERA-I and observations confirms the applicability of the ICON model for the sensitivity experiments of the main article.

Figure S1 shows average profiles of cloud cover (CLC), relative humidity (RH), horizontal wind speed v_{horiz} as well as specific cloud water content q_c for 00, 06, 12 and 18 UTC (corresponding to local time in our study region). At 00 UTC the NLLJ is already well established and the low-level cloud deck is beginning to form (Fig. S1a). ICON shows a considerably stronger jet than ERA-I reaching 7 ms^{-1} at 925-950 hPa and consistently lower values in CLC , RH and q_c . In contrast to ERA-I, ICON tends to concentrate cloud water in the upper parts of the cloud deck around 850 hPa. The relatively small differences in RH between the two datasets (more than 90% from 830 hPa downwards) in contrast to differences in CLC and q_c illustrates a substantial sensitivity to the subgrid-scale cloud scheme or possibly differences in spatial variance of RH , as the dependence of CLC on RH is quadratic in ICON. The tendency of stronger NLLJ and less cloud was also found in many climate models (Hannak et al. 2017). At midlevels around 560 hPa ICON shows a secondary peak in v_{horiz} , CLC , RH and q_c not found in the overall smoother and moister ERA-I profiles.

At 06 UTC the NLLJ is very similar to 00 UTC but the low-level cloud deck increases markedly in cover and q_c accompanied by an increase in RH to values well above 95 % below 900 hPa (Fig. S1b). Maximum CLC occurs at 950 hPa reaching 25% in ICON and about 45% in ERA-I, which is more realistic (cf. van der Linden et al., 2015). Overall the discrepancies between the two models are qualitatively similar to 00 UTC (Fig. S1a). At midday (Fig. S1c), radiative heating lifts and dissolves the low-level cloud deck shifting the maximum in CLC and RH to 850 hPa, where a pronounced peak in q_c develops. Surface heating and turbulent mixing markedly slows down the low-level jet (e.g. 4.5 ms^{-1} in ICON) and decreases RH to under 90% below 900 hPa with ICON being substantially drier and less cloudy in that layer. Finally at 18 UTC (Fig. S1d) the low-level jet starts re-accelerating, keeping the generally higher values in ICON found at all times of day. The deep daytime mixing has reduced CLC and q_c and created an almost vertically constant offset between the two modeling systems. RH is already increasing at this time of day, particularly in ICON, where also the sharp gradient in v_{horiz} suggests a beginning decoupling of the surface. Such an early evening transition is consistent with observations as documented in Fig. 3d in Schuster et al. (2013). The comparison between the two datasets shows considerable biases at all times of day with generally higher low- and midlevel wind maxima in ICON but moister and more cloudy low levels in ERA-I. Investigating the reasons for these discrepancies is beyond the scope of this paper but the overall agreement in vertical structure and diurnal cycle suggests that sensitivities tested with ICON should be qualitatively meaningful.

S1.2 Temporal stability of opacity-induced effects

An additional aspect to be discussed is the response time of the atmospheric system to the imposed cloud modifications. To investigate this we use EXPL experiments, in which $f_{op} = 0.1$ is applied for the first 4 days but then switched off for 6 more days of simulation time. Control runs with $f_{op} = 1.0$ for all times were produced for comparison. As in EXPL, simulations were started every 4th day but run out to 10 days and two starting dates in August were added (3rd and 7th of August) to give better statistics for the time evolution. Figure S2 shows box-averaged 10-day time-series of RR , cover of low clouds CLC_{low} and that of high clouds CLC_{high} (below 800 hPa and above 400 hPa, respectively) for the DACCIWA region (Figs. S2a-c). The corresponding differences between the two sets of simulations are provided in the right-hand side panels of Fig. S2.

After the switch-off at 12 UTC on the fifth simulation day (i.e. after 96 hours), the differences in SSI and low-level T are reduced almost immediately (not shown), but for other variables the response is slower. RR shows the enhancement of afternoon and evening precipitation for $f_{op} = 0.1$ as in EXPL (Figs. S2a and f). The enhancement is still fully visible for the first 14 hours after switch-off, indicating that the influence of the forcing during the morning hours is already enough to generate more instability and trigger more convection later in the day. After that, differences between the two runs become

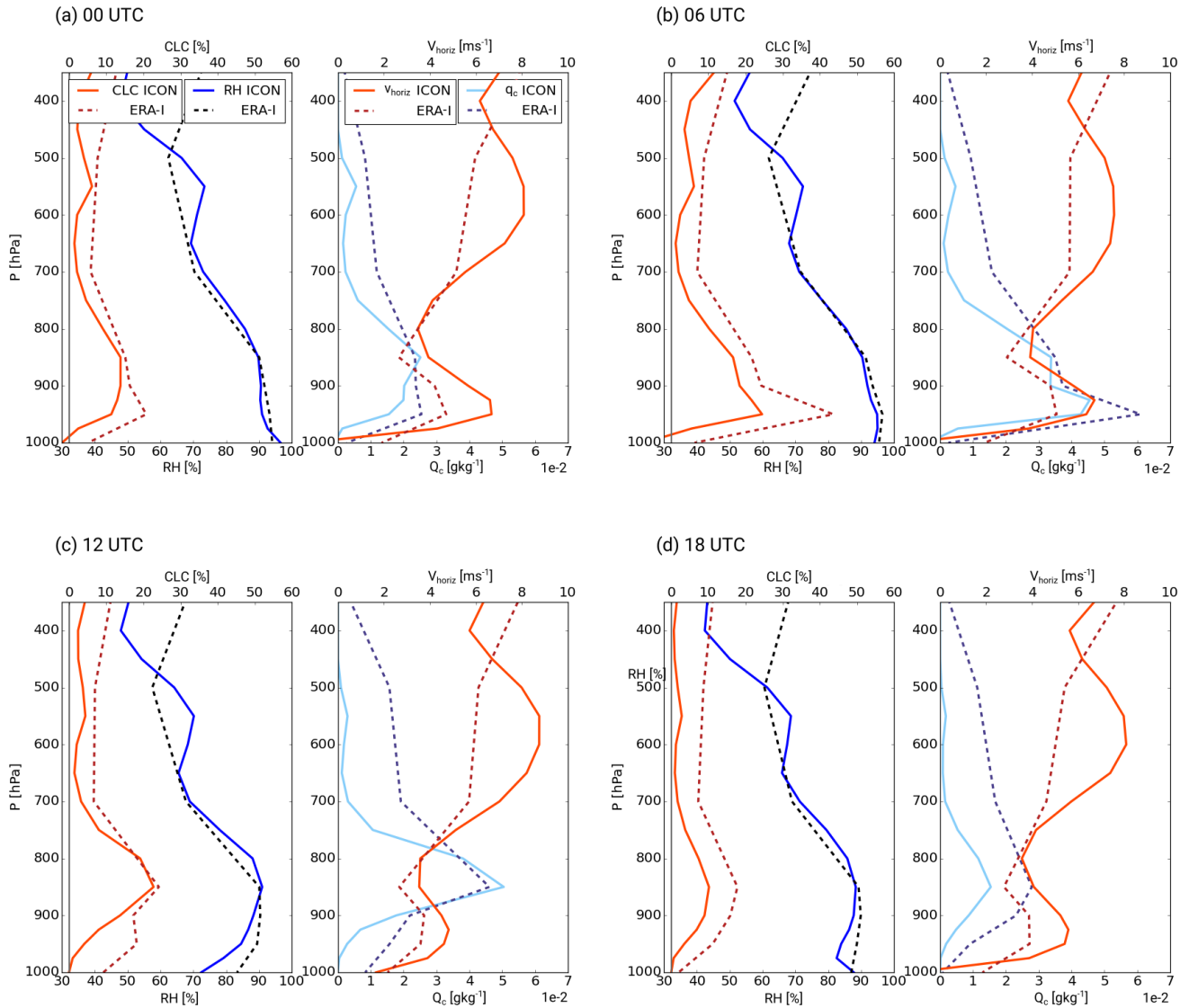


Figure S1. Average profiles of CLC and RH (left graph), v_{horiz} and components (middle graph) and q_c (right graph) for the monsoon season July - September. Averages over the DACCIWA area are shown as diurnal cycle where (a) is 00 UTC, (b) 06 UTC, (c) 12 UTC and (d) 18 UTC. Solid lines denote the ICON results with simulations started daily at 12 UTC and dashed lines denote the corresponding ERA-Interim fields.

negligible. Before the switch in f_{op} , CLC_{low} shows the familiar afternoon decrease and nighttime increase (Figs. S2b and g). On the day of the change, some signal remains until the morning of the following day, similar to RR . The small but on average slightly positive differences after that may be a reflection of increased surface fluxes after the strongly enhanced rainfall of the first five days. CLC_{high} (Figs. S2c and h) shows a considerably slower response. Differences between the two runs need one full diurnal cycle to establish and are then positive for the next three days. After the switch, there is a marked decrease

5

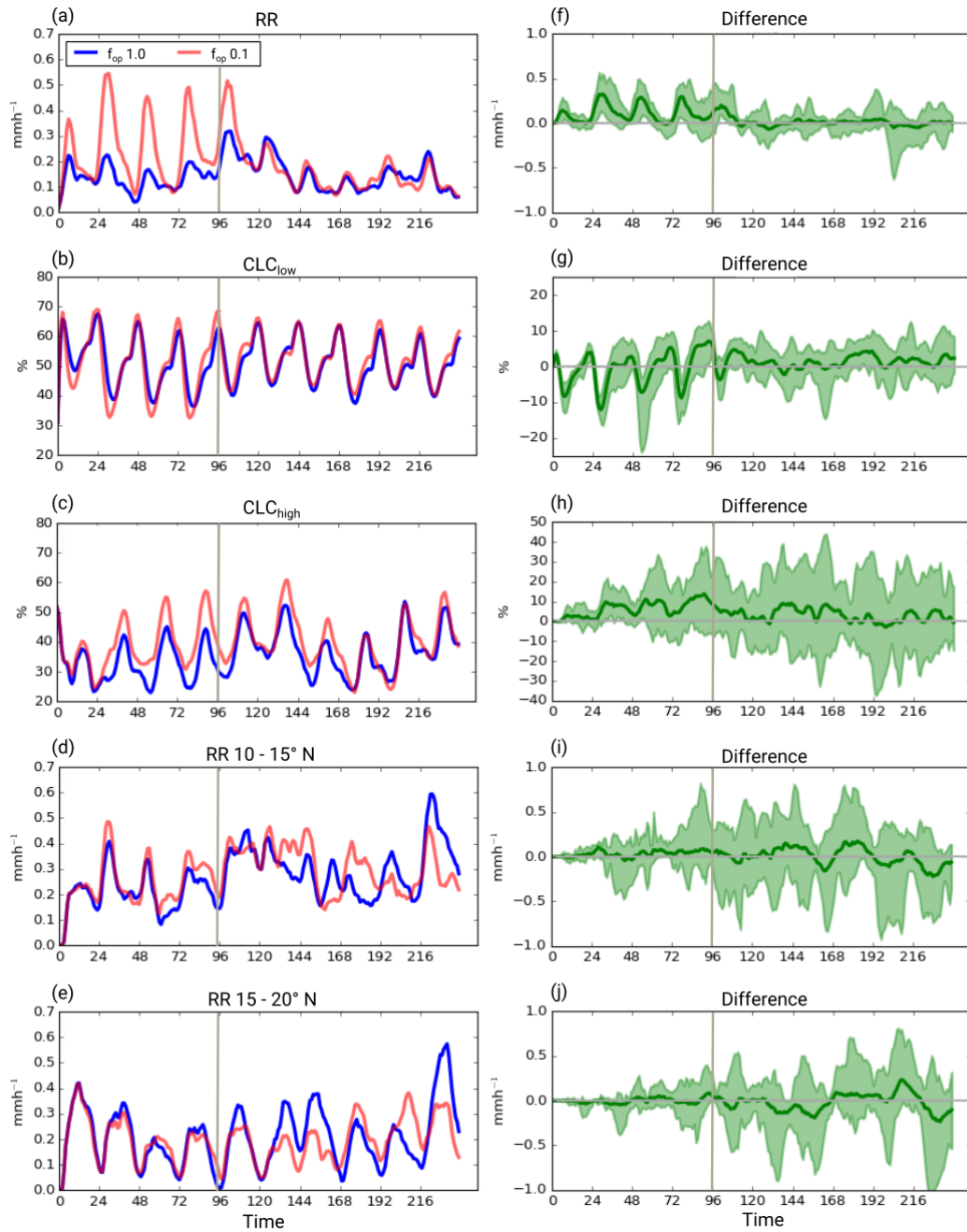


Figure S2. Time-series of RR (a), CLC_{low} (b) and CLC_{high} (c) of the experiments with $f_{op} = 1.0$ all the time (blue line) and f_{op} switched from 0.1 to 1.0 after 96 hours (orange line). Results are averaged over the DACCIWA box, for all 10 runs in July-August 2006. (d) and (e) depict similar averages of RR but for the northern boxes 15–20°N, 8°W–8°E and 15–20°N, 8°W–8°E, respectively. The corresponding differences are shown as green lines in (f)–(j), where the shaded area denotes the maximum and minimum values of the time-series. Switch-off time is indicated by a grey line in all panels.

in differences but then an overall tendency for relatively large values for two more days. This is consistent with Raymond et al. (2011), who show a considerably longer response time in the tropical upper troposphere than at low levels for a given perturbation.

5 Another interesting question is the impact on regions to the north, i.e. downstream of the DACCIWA box with respect to the monsoon flow. Figures S2d, e, i and j show corresponding plots for RR over the Sahelian regions $10\text{--}15^\circ\text{N}$ and $15\text{--}20^\circ\text{N}$, both averaged over $8^\circ\text{W}\text{--}8^\circ\text{E}$. For the former, again an initial response time of about one day is observed followed by a period of small positive differences. During the last five days of the simulation there is then no clear net difference between the two sets of experiments but much larger fluctuations. As these do not follow a strict diurnal cycle, we speculate that this is mostly a reflection of the overall chaotic nature of the atmosphere growing with leadtime. This conclusion is consistent with the similar
10 behavior found for the $15\text{--}20^\circ\text{N}$ band.

So in summary, this experiment shows that low-level variables such as SSI and T react almost immediately to changes in low cloud during the day. Low-level cloud cover and rainfall respond after one full diurnal cycle, while upper-level variables and neighboring regions show even longer responses, but also increasingly chaotic behavior. The latter is reflected in the growing shaded areas denoting the envelope of all runs in the bias in the right-hand side panels of Fig. S2.

15

S1.3 Table of acronyms

Table S1. Table of acronyms and abbreviations used in the main article.

Acronym	denotation
θ_e	equivalent potential temperature
CALIPSO	Cloud-Aerosol Lidar and Infrared Pathfinder Satellite Observation
CERES	Clouds and the Earth's Radiant Energy System
CM SAF	Satellite Application Facility on Climate Monitoring
CLC	cloud cover
CLC_{low}	low-cloud cover
CLC_{high}	high-cloud cover
CloudSat	satellite in A-train with cloud profiling radar
COSMO model	Consortium for Small-scale Modeling model
COSMO-EU	regional COSMO model for Europe
DACCIWA	Dynamics-Aerosol-Chemistry-Cloud Interactions in West Africa project
DWD	German weather service
EBAF-Surface	Energy Balanced And Filled surface irradiance
EBAF-TOA	Energy Balanced And Filled top of atmosphere irradiance
ECMWF	European Centre for Medium-Range Weather Forecasts
ERA-I	ERA Interim
EXPL	experiment with explicit convection
f_{op}	opacity factor
GERB	Geostationary Earth Radiation Budget
GPCP	Global Precipitation Climatology Project
GPCC	Global Precipitation Climatology Centre
ICON	Icosahedral Non-hydrostatic (numerical weather prediction model of DWD)
IFS	Integrated Forecasting System
ITD	Intertropical Discontinuity
MODIS	Moderate Resolution Imaging Spectroradiometer
MPI-M	Max Planck Institute for Meteorology
MVIRI	Meteosat Visible and Infrared Imager
NLLJ	nocturnal low-level jet
NPP	Suomi National Polar-orbiting Partnership
NWP	numerical weather prediction
OLR	outgoing longwave radiation

Acronym	denotation
<i>OSR</i>	outgoing shortwave radiation
<i>p_{sf_c}</i>	surface pressure
PARAM	experiment with parameterised convection
PBL	planetary boundary layer
<i>q_c</i>	cloud liquid water content
<i>q_i</i>	cloud ice content
<i>q_v</i>	specific humidity
<i>RH</i>	relative humidity
<i>RR</i>	precipitation rate
RRTM	Rapid Radiation Transfer Model
SARAH	Surface Solar Radiation Data Set Heliosat
SEVIRI	Spinning Enhanced Visible and InfraRed Imager
SLEVE	smooth level vertical (coordinate)
<i>SLI</i>	surface longwave irradiance
SOCRATES	Suite Of Community RAdiative Transfer codes based on Edwards and Slingo
<i>SSI</i>	solar surface irradiance
<i>SST</i>	sea surface temperature
SWA	southern West Africa
SWITCH	experiment where opacity factor is switched to 1 after some time
<i>T</i>	temperature
TERRA	soil and vegetation model
<i>TKE</i>	turbulent kinetic energy
TMPA	TRMM Multisatellite Precipitation Analysis
TOA	top of atmosphere
TRMM	Tropical Rainfall Measuring Mission
<i>v_{horiz}</i>	horizontal wind speed
WAM	West African monsoon